

# Whole-body immunoPET reveals active SIV dynamics in viremic and antiretroviral therapy–treated macaques

Philip J Santangelo<sup>1</sup>, Kenneth A Rogers<sup>2</sup>, Chiara Zurla<sup>1</sup>, Emmeline L Blanchard<sup>1</sup>, Sanjeev Gumber<sup>3,4</sup>, Karen Strait<sup>5</sup>, Fawn Connor-Stroud<sup>5</sup>, David M Schuster<sup>6</sup>, Praveen K Amancha<sup>2</sup>, Jung Joo Hong<sup>2</sup>, Siddappa N Byrareddy<sup>4</sup>, James A Hoxie<sup>7</sup>, Brani Vidakovic<sup>1</sup>, Aftab A Ansari<sup>4</sup>, Eric Hunter<sup>4</sup> & Francois Villinger<sup>2,4</sup>

**The detection of viral dynamics and localization in the context of controlled HIV infection remains a challenge and is limited to blood and biopsies. We developed a method to capture total-body simian immunodeficiency virus (SIV) replication using immunoPET (antibody-targeted positron emission tomography). The administration of a poly(ethylene glycol)-modified, <sup>64</sup>Cu-labeled SIV Gp120-specific antibody led to readily detectable signals in the gastrointestinal and respiratory tract, lymphoid tissues and reproductive organs of viremic monkeys. Viral signals were reduced in aviremic antiretroviral-treated monkeys but detectable in colon, select lymph nodes, small bowel, nasal turbinates, the genital tract and lung. In elite controllers, virus was detected primarily in foci in the small bowel, select lymphoid areas and the male reproductive tract, as confirmed by quantitative reverse-transcription PCR (qRT-PCR) and immunohistochemistry. This real-time, *in vivo* viral imaging method has broad applications to the study of immunodeficiency virus pathogenesis, drug and vaccine development, and the potential for clinical translation.**

Delineating viral replication in the context of generalized infections has traditionally relied on indirect measures, such as evaluating viral loads in plasma or via specific tissue biopsies. Such approaches have been valuable for the clinical management of viral infections, although they generally do not identify the site or source of virus replication *in vivo*. In a small percentage of HIV-infected individuals termed elite controllers (ECs), virus replication is controlled to undetectable levels without antiretroviral intervention, and disease progression may be delayed for decades<sup>1,2</sup>. Despite undetectable virus in the plasma, virus evolution continues to occur consistently with ongoing tissue-contained virus replication<sup>3,4</sup>. It is critical to identify tissue sites

that can possibly serve as viral reservoirs so that the mechanisms by which such reservoirs are maintained can be identified. This would facilitate the development of strategies for eliminating these reservoirs, particularly in individuals treated with highly active antiretroviral therapy (ART)<sup>5</sup>. Ideally, a method to identify changes in virus localization would be minimally invasive as well as specific, sensitive and amenable to repeated application. Here we describe the application of whole-body imaging to the detection and localization of sites of SIV infection in chronically infected, ART-treated and EC macaques.

## RESULTS

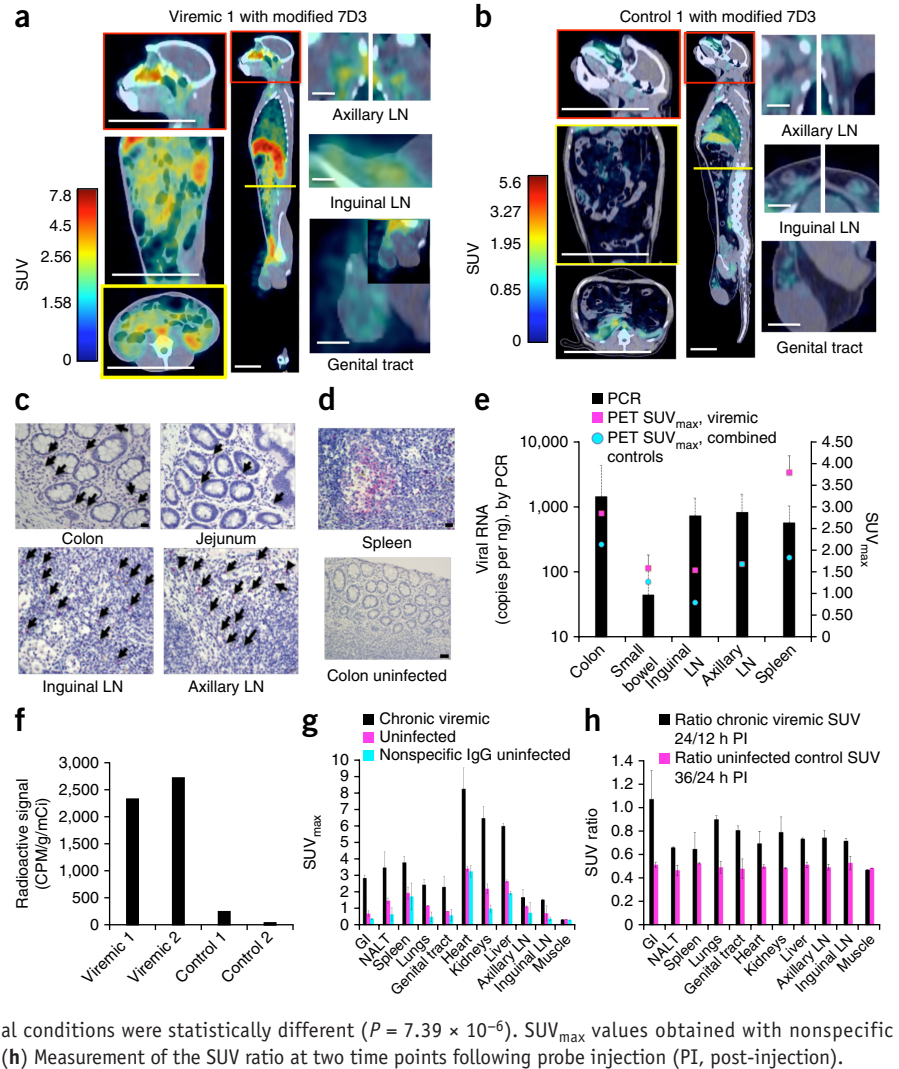
We hypothesized that the higher sensitivity and image quality of <sup>64</sup>Cu-based positron emission tomography (PET) over that of single-photon emission computer tomography<sup>6</sup> could be exploited to detect the major target tissues infected by SIV or HIV by scanning the entire body<sup>7–10</sup>. To test this hypothesis, we employed the SIV-infected rhesus macaque as a model of pathogenic HIV infection<sup>11,12</sup> and chose the glycoprotein Gp120 as the *in vivo* target<sup>7</sup>.

## Development of the immunoPET probe

We selected the SIV Env protein-specific monoclonal antibody (mAb) clone 7D3 as the basis of the probe because of its broad SIV Env specificity<sup>13–15</sup>. 7D3 binds the CCR5 binding site of Gp120 and prevents syncytia formation *in vitro* with SIV<sub>MACCP-MAC</sub>, although it does not affect soluble CD4 binding or neutralize SIV<sub>mac239</sub> (ref. 13). Furthermore, three 7D3 molecules can bind to the trimeric Env of SIV<sub>MACCP-MAC</sub> and SIV<sub>MAC239</sub> (ref. 15). To mitigate the immunogenicity of murine antibodies (probe antibodies were not detected after two administrations; data not shown), decrease nonspecific interactions and enable the chelation of <sup>64</sup>Cu, the mAb was modified with linear 10-kDa

<sup>1</sup>Wallace H. Coulter Department of Biomedical Engineering, Georgia Institute of Technology and Emory University, Atlanta, Georgia, USA. <sup>2</sup>Division of Microbiology and Immunology, Yerkes National Primate Research Center, Emory University, Atlanta, Georgia, USA. <sup>3</sup>Division of Pathology, Yerkes National Primate Research Center, Emory University, Atlanta, Georgia, USA. <sup>4</sup>Department of Pathology and Laboratory Medicine, Emory University School of Medicine, Atlanta, Georgia, USA. <sup>5</sup>Division of Veterinary Medicine, Yerkes National Primate Research Center, Emory University, Atlanta, Georgia, USA. <sup>6</sup>Department of Radiology and Imaging Sciences, Emory University School of Medicine, Atlanta, Georgia, USA. <sup>7</sup>Department of Medicine, University of Pennsylvania School of Medicine, Philadelphia, Pennsylvania, USA. Correspondence should be addressed to F.V. (fvillin@emory.edu).

**Figure 1** | PET/CT results from uninfected control and four chronically SIV infected, viremic rhesus macaques. **(a,b)** Frontal, sagittal and axial views and magnifications of a viremic monkey, Viremic 1, and of a representative uninfected monkey, Control 1, imaged with the modified 7D3 probe. Sites of axial sections are marked by a yellow line within the sagittal view. Scale bars (white): axial and frontal view of torso and sagittal view of head, 100 mm; sagittal view of whole body, 50 mm; lymph nodes (LN) and genital tract, 20 mm. **(c,d)** IHC against SIV Gag in tissues from Viremic 1 **(c)** and in spleen from an SIV-infected monkey with high viremia and in uninfected colon control tissues **(d)**. Arrows indicate infected mononuclear cells. Scale bars: colon uninfected **(d)**, 50  $\mu$ m; all other images **(c,d)**, 20  $\mu$ m. **(e)** Quantification of the PET data from various tissues from 4 SIV-infected and viremic monkeys (magenta) as well as 2 uninfected monkeys administered the 7D3 probe and 2 monkeys administered an isotype IgG probe (blue). The maximum standard uptake value ( $SUV_{max}$ ) within each organ was compared directly with the qRT-PCR results. Mean  $\pm$  s.d. shown for PET and SIV RNA copies for each organ across all animals tested. **(f)** Rectal biopsy results from 2 chronically infected and 2 uninfected animals. Activity is reported in counts per min (CPM) adjusted for tissue weight and the activity of the injected probe. **(g)** Comparison of  $SUV_{max}$  results in the same viremic and uninfected monkeys as in **e**; a repeated measures ANOVA confirmed that the animal conditions were statistically different ( $P = 7.39 \times 10^{-6}$ ).  $SUV_{max}$  values obtained with nonspecific IgG control in uninfected animals are also included. **(h)** Measurement of the SUV ratio at two time points following probe injection (PI, post-injection).



poly(ethylene glycol) (PEG)<sup>16</sup> through standard succinimidyl ester–amino chemistry and the chelator DOTA NHS (1,4,7,10-tetraazacyclododecane-1,4,7,10-tetraacetic acid mono), which has been demonstrated to be stable in humans and mice for at least 72 h (refs. 17,18).

We performed *in vitro* assays to validate the probe (**Supplementary Fig. 1**). First, we incubated the <sup>64</sup>Cu-labeled radiotracer with varying percentages of SIV1C cells and uninfected Hut78 cells (**Supplementary Fig. 1a**), demonstrating a linear binding response with decreasing percentages of infected cells, as measured with a gamma counter. Next we measured gamma counts from equal aliquots of cryopreserved and thawed splenocytes and lymph node cells, collected at necropsy from uninfected and SIV-infected animals (**Supplementary Fig. 1b**). The data demonstrate that even after a freeze-thaw cycle, the 7D3-PEG-<sup>64</sup>Cu-DOTA probe bound specifically to infected cells. Subsequently, we performed a competition assay whereby ‘cold’ 7D3-PEG-DOTA was used to compete with bound ‘hot’ 7D3-PEG-<sup>64</sup>Cu-DOTA from SIV1C and Hut78 cells, demonstrating epitope-specific binding of the probe (**Supplementary Fig. 1c**). In order to assess differences between 7D3-PEG-DOTA- and 7D3-PEG-DyLight 650-labeled probes (used in flow cytometry assessments), we used both probes to label SIV1C cells,

demonstrating specific binding (**Supplementary Fig. 1e**). This experiment showed that the fluorescent probe binds with the same efficacy as the 7D3-PEG-DOTA (cold) probe. We then assessed the DyLight 650-labeled probe, using flow cytometry for its binding to SIV1C cells in the presence of serum and SIV-specific antibodies generated during infection (**Supplementary Fig. 1f**). Although there was less binding of 7D3 in the presence of the pre- and post-infection serum than with monkey serum absent, we noted specific binding to SIV1C relative to uninfected Hut78 cells.

### Characterization of chronic SIV infection

To generate images of SIV dissemination *in vivo*, we injected the 7D3-PEG-<sup>64</sup>Cu-DOTA probe (labeled with 1–3.5 mCi/mg <sup>64</sup>Cu) into rhesus macaques intravenously. We tested probe stability by pelleting virus from the plasma of the infected and uninfected animals and measuring the radioactivity (**Supplementary Fig. 1d**). These data demonstrate that specific probe binding to virus was still possible 24 h after injection of the probe. We found PET and computed tomography (CT) imaging (hereafter PET/CT) in both viremic and control animals to be optimal 24–36 h after injection (data not shown). We then imaged macaques chronically infected with SIV<sub>MAC239</sub> and uninfected control

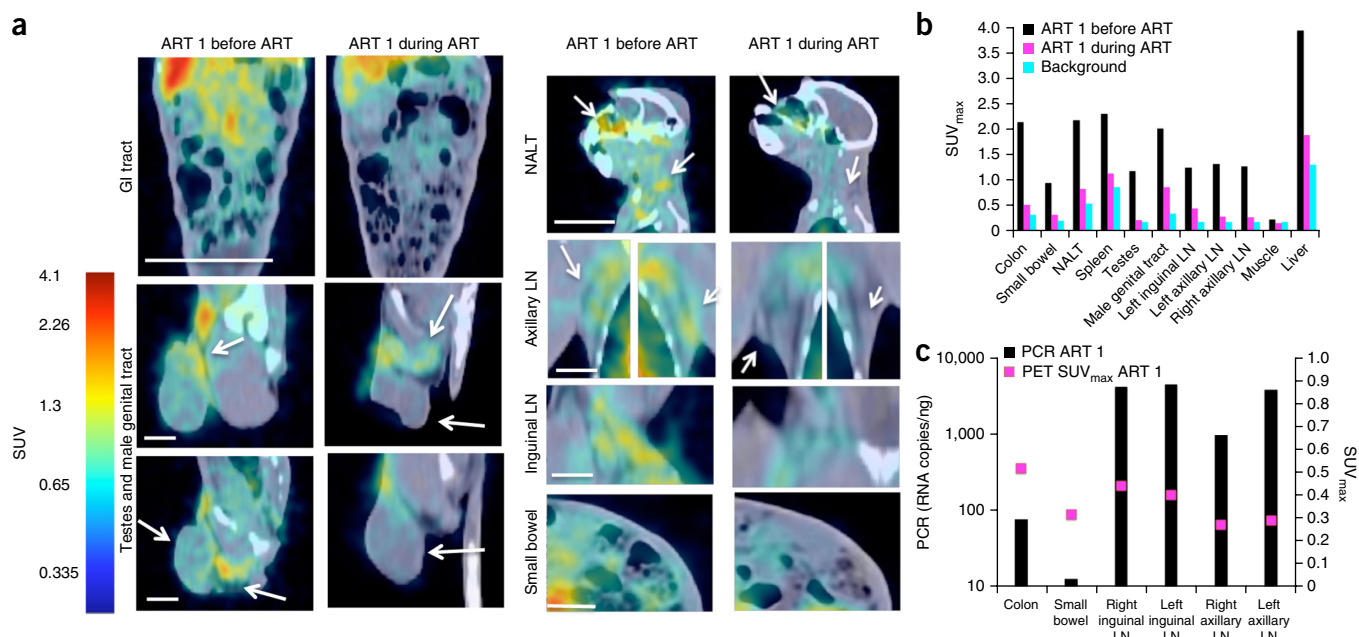


**Figure 2** | PET/CT results from a chronically infected macaque, before and at 5 weeks of ART. **(a)** Standard uptake value (SUV) maps of GI tract, lymph nodes (LN), genital tract, spleen and small bowel. NALT, nasal-associated lymphoid tissue. Arrows indicate areas for which specific PET signals decreased during ART. Scale bars: frontal view of torso, 100 mm; sagittal view of head, 50 mm; LN and genital tract, 20 mm; small bowel, 15 mm. **(b)** SUV<sub>max</sub> values before and after 5 weeks of ART compared with background uptake in 2 uninfected animals. **(c)** qRT-PCR verification of residual virus compared with SUV<sub>max</sub> PET data at 5 weeks of ART in one representative treated macaque.

animals after injection with either a  $^{64}\text{Cu}$ -labeled, PEG-modified 7D3 mAb or a similarly labeled control IgG to test the ability of the modified mAb to specifically target and detect SIV-infected cells and tissues *in vivo*, displaying frontal, sagittal and axial images (Fig. 1a,b, Supplementary Fig. 2a–f and Supplementary Table 1). We generated standardized uptake value (SUV) maps for each PET and corresponding CT image using OsiriX software (Fig. 1a,b and Supplementary Fig. 2a–f). SUV is essentially the measured activity within a region of interest, normalized by the radioactive dose divided by the subject's weight. In the viremic animals, SUV values greater than those observed in the control cases were localized to the gastrointestinal (GI) system, specifically within the ileum, jejunum and colon, and the axillary and inguinal lymph nodes, correlating with previously reported findings<sup>12,19–21</sup>. We also detected uptake within the lungs, a less well-characterized site of viral infection<sup>22</sup>. As can be seen in detail in slice sequences for monkeys Viremic 1 and 2, the uptake followed the contours of the ileum and colon (Supplementary Fig. 3a,b). We also consistently detected antibody uptake within the nasal cavity, likely reflective of the nasal-associated lymphoid tissue (NALT) or nasal turbinates (Fig. 1a), an area that has received little attention as a source of viral replication. In males, we frequently observed uptake within the genital tract, specifically in the vas deferens and epididymis, corroborating previous reports<sup>23–25</sup>. In contrast to a previous report<sup>26</sup>, infection of epithelial cells was not detected in the male genital organs. In the uninfected monkeys, background was evident within the liver, heart, kidneys and spleen, which is typical of antibody-based radiotracers<sup>17,18</sup>. It should be noted, however, that SUVs were significantly higher in infected animals than in control cases in each of these organ systems, indicating specific uptake ( $P < 0.05$ , Kruskal-Wallis test; Supplementary Table 2). A sequence of frontal slice images

obtained on the uninfected monkey Control 1 after administration of  $^{64}\text{Cu}$ -7D3 demonstrates that uptake was minimal throughout the GI tract and that background was restricted to the heart, liver, kidneys and spleen (Supplementary Fig. 3c).

### PET quantification and comparison with qRT-PCR and IHC

We verified the imaging signal data by qRT-PCR and through the examination of sections of the specific tissue of interest using immunohistochemistry (IHC) for SIV Gag protein (Fig. 1c,d and Supplementary Fig. 2). These confirmatory studies used rectal biopsy tissues obtained immediately after imaging and/or tissues obtained post-mortem. On the basis of the IHC data, the GI tract, lymph nodes and spleen all contained infiltrating SIV-infected cells of lymphocyte or macrophage morphology. Negative control tissue (Fig. 1d) did not contain any detectable signal using the same IHC protocol. We also performed qRT-PCR using tissue samples from the colon, small bowel, spleen and inguinal and axillary lymph nodes for all of the chronically infected animals and controls (Fig. 1e). Corroborating our IHC results, we detected viral RNA in all cases, with the highest levels in the colon; we did not detect RNA in the controls. In addition, we quantified the  $^{64}\text{Cu}$ -radioactivity associated with aliquots of rectal biopsies from viremic monkeys Viremic 1 and 2 and uninfected Controls 1 and 2 with a gamma counter. The signal from these tissues, normalized for the mass of the biopsy and the total amount of radioactivity administered, was 17.6 times higher on average in infected animals (Fig. 1f) than in both controls, providing additional confirmation of the specificity of the PET imaging.

To compare the PET results from viremic animals to those of the controls, we quantified the data using SUV (Fig. 1a,b,e,g and Supplementary Fig. 2). We chose volumes of interest in the PET/CT fusion images by outlining the organ manually in the CT

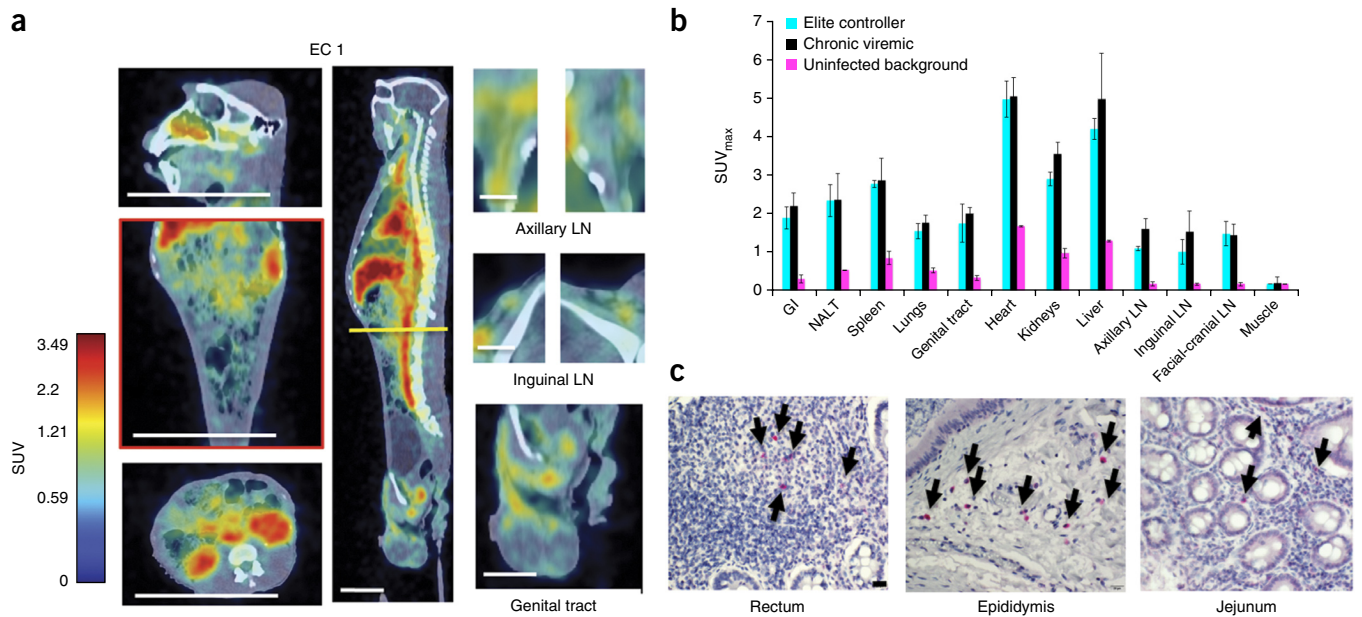


**Figure 3** | PET/CT results from SIV-infected elite controllers (ECs). **(a)** Frontal, sagittal and axial views and magnifications from one SIV-infected EC macaque 36 h after injection of the labeled antibody. The axial section is denoted by a yellow line within the sagittal view. Macaque EC 1 was infected for over 6 years and displayed plasma viral loads of fewer than 60 copies of viral RNA per ml for the last 5 years. Scale bars (white): axial and frontal view of torso and sagittal view of head, 100 mm; sagittal view of whole body, 50 mm; lymph nodes (LN) and genital tract, 20 mm. **(b)** SUV<sub>max</sub> quantification results from the PET/CT imaging, comparing 4 viremic and 4 EC monkeys with 2 uninfected controls (mean  $\pm$  s.d.). See **Supplementary Note** for a description of the statistical analysis of this data. **(c)** IHC results against the SIV<sub>MAC239</sub> Gag for macaque EC 1. Arrows indicate infected mononuclear cells in select tissue biopsies. Scale bar, 20  $\mu$ m.

images throughout the image slices. Using the organ volume as the region of interest (ROI), we then determined the maximum SUV within that organ and compared the SUV<sub>max</sub> within viremic and uninfected animals with the qRT-PCR results from the corresponding colon, small bowel, spleen and inguinal and axillary lymph nodes of the same animal (**Fig. 1e**). These data suggest that the PET SUV<sub>max</sub> values mimic the general trends of the PCR data. For the spleen, which tends to have higher background uptake, the SUV<sub>max</sub> minus background is a more relevant comparison with the qRT-PCR data. It should be pointed out that the SUV data are unlikely to match the PCR data precisely, as protein and RNA expression levels may differ.

Next, to address the specificity of the PET signals, we compared the SUV<sub>max</sub> measurements for various tissues from chronically infected and uninfected macaques injected with either the modified 7D3-labeled antibody or with a labeled isotope control antibody (**Fig. 1g** and **Supplementary Fig. 2g**). The data suggest that there is increased uptake within organ systems likely to contain virus or virally infected cells and tissue. For each group of animals, we then performed an overall comparison of the PET measurements that included the signals of all organs, applying a fully nested hierarchical ANOVA model for the SUV<sub>max</sub> response. The null hypothesis for the comparison was that the viral status of the animal and the injected probe would not influence the imaging results. We found that the viremic animals were significantly different from the uninfected controls ( $P = 7.39 \times 10^{-6}$ ). However, animals within each group, infected or uninfected, were not significantly different from each other ( $P = 0.89$ ). The analysis also showed that both the infection status (animal group) and organs contributed significantly to the SUV<sub>max</sub> value. We found that for the chronically viremic

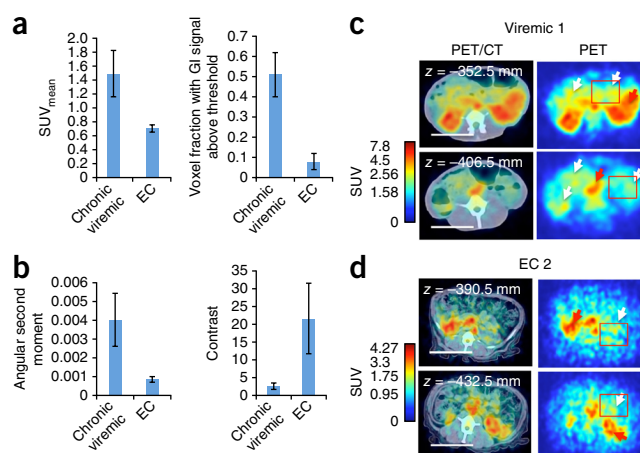
animals and both control groups, the measurements for each organ within each group were significantly different from each other, yielding  $P$  values of  $1.4 \times 10^{-9}$ ,  $7.1 \times 10^{-27}$  and  $4.78 \times 10^{-19}$ , respectively. Furthermore, when we applied the Kruskal-Wallis test for each organ separately (**Supplementary Table 2**), the signals measured in viremic and uninfected controls were statistically distinct except for in muscle.

Another method of assessing specific uptake for a particular organ is to examine the dynamics of uptake. Owing to logistics, we scanned animals at 12, 24 and/or 36 h after injection and plotted the ratios of the average SUV<sub>max</sub> values at each time point for each organ (**Fig. 1h**). When we compared the viremic monkeys with the aviremic controls, all of the ratios in viremic animals were higher—typically above 0.6, with the GI tract giving values  $>1.0$ —indicating continued specific uptake of the probe. The decay rate and SUV<sub>max</sub> values in whole blood (SUV<sub>max</sub>  $\approx$  0.3–0.4; data not shown) were similar to those of muscle, and remained similar between groups. We did not detect uptake in the central nervous system, probably because of probe exclusion by the blood-brain barrier<sup>27</sup>.

### SIV localization before and during antiretroviral therapy

In order to confirm the sensitivity of this method and its ability to track SIV replication anatomically during treatment, we first imaged three chronically infected animals (ART 1, ART 2 and ART 3) 36 h after injection with our modified 7D3 probe and then initiated them on ART (20 mg PMPA (9-(2-phosphonomethoxypropyl) adenine) per kg body weight per day (mg per kg per d) and 50 mg per kg per d emtricitabine (FTC) each subcutaneously and 100 mg/d for 40 d of integrase inhibitor L-870812) (**Fig. 2** and **Supplementary Fig. 4**). All three animals were aviremic by

**Figure 4** | Comparison of viremic with elite controller (EC) macaques. (a) Comparison of  $SUV_{\text{mean}}$  and  $SUV_{\text{voxel}}$  fraction (fraction of total volume of GI tract) within the GI tract of 4 chronic SIV-positive and 4 EC macaques. The voxel fractions that contained SUVs above 1 and below 3.3 (excludes interfering signals) were included. (b) Haralick texture function measurements of angular second moment and contrast for regions of interest (ROIs; depicted by red boxes in c,d). The angular second moment is a measure of homogeneity, whereas the contrast metric represents the local variations within an image or ROI. Data reported as mean  $\pm$  s.d. (c,d) Representative axial cross sections of a chronically infected macaque (Viremic 1) and one controller macaque (EC 2). Red arrows indicate uptake within the liver; white arrows in c point toward the GI tract; white arrows in d point to mesenteric lymph nodes and other foci. Scale bars, 50 mm.



3–4 weeks of treatment (having viral loads <60 copies of RNA per ml; **Supplementary Fig. 5**) and imaged again after 5 weeks on ART (**Fig. 2** and **Supplementary Fig. 4**). Prior to treatment, there was measurable SIV signal localized within the GI tract, NALT, genital tract and axillary and inguinal lymphoid tissue. After 34 d of treatment, all organ systems exhibited decreased uptake (**Fig. 2a,b**, **Supplementary Fig. 4** and **Supplementary Table 3a**). However, there was residual signal (above the background) in all organ systems, with moderate  $SUV_{\text{max}}$  values still remaining in the colon, spleen, male genital tract, NALT and individual lymph nodes for specific animals. In none of the cases did the  $SUV_{\text{max}}$  decrease to our measurable limit (background). To assess the statistical significance of the  $SUV_{\text{max}}$  measurements, we performed a hierarchical ANOVA analysis as described above. The differences between the  $SUV_{\text{max}}$  data before and after treatment from all of the organs imaged were significant, with a  $P$  value of 0. In a pairwise comparison, ART 1 and ART 3 were significantly different from ART 2 ( $P = 0.0027$ ), demonstrating the individual variation in ART treatment.

To verify the imaging results, we performed qRT-PCR on multiple tissue samples and compared the data directly with  $SUV_{\text{max}}$  data (**Fig. 2c** and **Supplementary Fig. 4c**). The samples included colon, small bowel, spleen, and right and left inguinal and axillary lymph nodes; these were collected at necropsy performed after 39 or 40 d on ART. Even though our PET procedure measures Env protein and qRT-PCR detects viral RNA, residual virus or infected cells were indeed present in the locations identified by PET. Both the spatial variation within an animal and the variation between animals suggested by PET was confirmed with qRT-PCR data (**Supplementary Fig. 6** and **Supplementary Table 3b**), with two-orders-of-magnitude variation within an organ and between animals. Additionally, the nasal turbinate, genital tract and lung samples were all positive for viral RNA (**Supplementary Table 3b**), indicating virus localization during both chronic and treated conditions, a similar result to that observed in viremic animals.

### SIV localization in elite controllers

We then applied the methodology to SIV-infected ECs. ECs are individuals that naturally suppress SIV (or HIV) replication to undetectable levels in plasma for extended periods of time without antiretroviral intervention<sup>1,2</sup>. Given the challenges studying viral persistence in these animals, they were an ideal test for our approach. EC monkeys exhibited detectable uptake (**Fig. 3** and **Supplementary Fig. 7**) within the GI tract, genital tract, NALT, lungs, spleen and axillary lymph nodes. These imaging data were supported by IHC in biopsy samples (**Supplementary Fig. 7**,

**Supplementary Table 2** and **Supplementary Note**). In ECs, the uptake was restricted to smaller regions or foci as compared to viremic animals. When quantified, the  $SUV_{\text{max}}$  organ signal appeared to approximate the results in viremic animals (**Fig. 3b**). However, when we applied a hierarchical ANOVA, we found that overall the PET  $SUV_{\text{max}}$  data for the viremic animals were statistically distinct from those of the ECs and the control animals ( $P = 2.78 \times 10^{-5}$ ). To clarify the differences between the ECs and viremic animals, we measured the  $SUV_{\text{mean}}$  within the GI tract and compared the voxel fractions (fraction of total volume of GI tract) (**Fig. 4** and **Supplementary Fig. 8**). The GI tract values in the viremic animals were 2.1 and 6.38 times greater than in the EC animals for  $SUV_{\text{mean}}$  and voxel fraction, respectively. Thus, although the viremic macaques and ECs had regions of comparably high uptake, in ECs, this was spatially restricted to much smaller volumes, and therefore the overall probe uptake was lower. We calculated additional metrics quantifying the spatial distributions within the GI tract, which further supported this conclusion (**Fig. 4a,b** and **Supplementary Note**).

### DISCUSSION

We describe the development of a non-invasive, sensitive immuno PET radiotracer and an approach to define the localization of SIV-infected tissue and free virus within live, chronically viremic, ART-treated and EC animals. The method can be repeated within the same animals (for example, before and during ART) without any adverse effect. In viremic animals, infection was concentrated within the mucosa of the gut, reiterating that these tissues are a major site of SIV replication<sup>12,20,21</sup>. However, we also observed discrete areas of virus replication, confirmed by qRT-PCR and IHC, both in nasal-associated tissues (post-ART) and in the reproductive tract of male animals. Within chronically infected, aviremic, ART-treated as well as EC animals, the methodology was able to detect residual virus, corroborated by qRT-PCR data. Thus, this approach provides the ability to identify novel areas of virus replication that may otherwise be difficult to sample in live animals. It may also provide a powerful tool to monitor the kinetics of viral replication in tissues over time during the application of novel therapeutic approaches. With the current efforts toward HIV eradication or functional cure, we believe that this method can be useful for determining organ-specific efficacy, which is crucial to the elimination of virally infected cells.

Our data also indicate that care must be taken when analyzing biopsies from aviremic subjects, especially ART-treated subjects, which may result in erroneous conclusions due to sampling (Supplementary Fig. 6 and Supplementary Table 3b). The detailed study of the cellular composition of these specific foci of infection, combined with site-specific drug metabolite levels and aided by the ability to image these specific sites, will likely be key to the development of directed therapies aimed at clearing infection from these sites in both controllers and individuals under ART<sup>28–30</sup>.

Although additional refinements to improve contrast and uptake are ongoing, we think that the methodology should be translatable to humans in the future because of the availability of anti-Env HIV antibodies<sup>31</sup> and because the imaging approach is based on technologies already used in the clinic<sup>17,18</sup>. It is applicable for studies investigating the eradication of HIV infection and targeting of virus reservoirs<sup>28,32</sup>. Moreover, use of this technology during acute SIV infection may provide improved delineation of spatial kinetics of viral spread based on the route of infection and allow the identification of stages at which interruption of infection may be targeted using prophylactic methods<sup>33</sup>.

## METHODS

Methods and any associated references are available in the [online version of the paper](#).

Note: Any Supplementary Information and Source Data files are available in the [online version of the paper](#).

## ACKNOWLEDGMENTS

We thank the animal and care staff of the Yerkes National Primate Research Center; B. Lawson, E. Strobert, J. Wood, S. Jean and M. Thompson; and D. Votaw and the Emory Clinic imaging team for their help in the conduct of these studies. Funding for these studies was provided by a developmental grant from the Yerkes National Primate Research Center, the Georgia Research Alliance, US National Institute of Allergy and Infectious Diseases grants R21-AI095129 to P.J.S. and F.V., R01 AI078775 and 8R24 OD010947 to F.V. and R01 AI078773 to A.A.A., the Center for AIDS Research P30 AI050409 and the base grant P51 OD11132 in support of Yerkes. E.H. is supported by a Georgia Research Alliance Eminent scholarship. We also thank M. Miller (Gilead Inc.) for the PMPA and FTC and D. Hazuda (Merck) for the integrase inhibitor. We gratefully acknowledge the help, support, encouragement and advice of O. Sharma (NIAID) given during the course of these studies.

## AUTHOR CONTRIBUTIONS

P.J.S., E.H. and F.V. conceived of the project. C.Z. produced the imaging agent, and P.J.S. and F.V. performed the radioactive labeling. P.J.S., F.V., C.Z., E.L.B., K.A.R., S.G., K.S., F.C.-S., P.K.A., J.J.H. and S.N.B. performed experiments. A.A.A. contributed animals and reagents. E.H. and J.A.H. provided reagents and advice. D.M.S. assisted with PET imaging. B.V. performed the statistical analyses. P.J.S., F.V., A.A.A. and E.H. wrote the manuscript.

## COMPETING FINANCIAL INTERESTS

The authors declare competing financial interests: details are available in the [online version of the paper](#).

Reprints and permissions information is available online at <http://www.nature.com/reprints/index.html>.

- Sáez-Cirión, A. *et al.* Post-treatment HIV-1 controllers with a long-term virological remission after the interruption of early initiated antiretroviral therapy ANRS VISCONTI Study. *PLoS Pathog.* **9**, e1003211 (2013).
- Zaunders, J. & van Bockel, D. Innate and adaptive immunity in long-term non-progression in HIV disease. *Front Immunol.* **4**, 95 (2013).
- Gray, L. *et al.* Phenotype and envelope gene diversity of *nef*-deleted HIV-1 isolated from long-term survivors infected from a single source. *Virology*. **4**, 75 (2007).
- Visco-Comandini, U., Aleman, S., Yun, Z. & Sönnnerborg, A. Human immunodeficiency virus type 1 variability and long-term non-progression. *J. Biol. Regul. Homeost. Agents* **15**, 299–303 (2001).
- Laird, G.M. *et al.* Rapid quantification of the latent reservoir for HIV-1 using a viral outgrowth assay. *PLoS Pathog.* **9**, e1003398 (2013).
- Di Mascio, M. *et al.* Noninvasive *in vivo* imaging of CD4 cells in simian-human immunodeficiency virus (SHIV)-infected nonhuman primates. *Blood* **114**, 328–337 (2009).
- Dadachova, E. *et al.* Targeted killing of virally infected cells by radiolabeled antibodies to viral proteins. *PLoS Med.* **3**, e427 (2006).
- Boerman, O.C. & Oyen, W.J. Immuno-PET of cancer: a revival of antibody imaging. *J. Nucl. Med.* **52**, 1171–1172 (2011).
- Fortin, M.A. *et al.* Immuno-PET of undifferentiated thyroid carcinoma with radioiodine-labelled antibody cMAb U36: application to antibody tumour uptake studies. *Eur. J. Nucl. Med. Mol. Imaging* **34**, 1376–1387 (2007).
- Lucignani, G. *et al.* FDG-PET imaging in HIV-infected subjects: relation with therapy and immunovirological variables. *Eur. J. Nucl. Med. Mol. Imaging* **36**, 640–647 (2009).
- Brenchley, J.M. & Paardini, M. Immunodeficiency lentiviral infections in natural and non-natural hosts. *Blood* **118**, 847–854 (2011).
- Lackner, A.A. & Veazey, R.S. Current concepts in AIDS pathogenesis: insights from the SIV/macaque model. *Annu. Rev. Med.* **58**, 461–476 (2007).
- Edinger, A.L. *et al.* Characterization and epitope mapping of neutralizing monoclonal antibodies produced by immunization with oligomeric simian immunodeficiency virus envelope protein. *J. Virol.* **74**, 7922–7935 (2000).
- White, T.A. *et al.* Three-dimensional structures of soluble CD4-bound states of trimeric simian immunodeficiency virus envelope glycoproteins determined by using cryo-electron tomography. *J. Virol.* **85**, 12114–12123 (2011).
- White, T.A. *et al.* Molecular architectures of trimeric SIV and HIV-1 envelope glycoproteins on intact viruses: strain-dependent variation in quaternary structure. *PLoS Pathog.* **6**, e1001249 (2010).
- Wattendorf, U. & Merkle, H.P. PEGylation as a tool for the biomedical engineering of surface modified microparticles. *J. Pharm. Sci.* **97**, 4655–4669 (2008).
- Mortimer, J.E. *et al.* Functional imaging of human epidermal growth factor receptor 2-positive metastatic breast cancer using <sup>64</sup>Cu-DOTA-trastuzumab PET. *J. Nucl. Med.* **55**, 23–29 (2014).
- Tamura, K. *et al.* <sup>64</sup>Cu-DOTA-trastuzumab PET imaging in patients with HER2-positive breast cancer. *J. Nucl. Med.* **54**, 1869–1875 (2013).
- Picker, L.J. Immunopathogenesis of acute AIDS virus infection. *Curr. Opin. Immunol.* **18**, 399–405 (2006).
- Heise, C., Vogel, P., Miller, C.J., Halsted, C.H. & Dandekar, S. Simian immunodeficiency virus infection of the gastrointestinal tract of rhesus macaques. Functional, pathological, and morphological changes. *Am. J. Pathol.* **142**, 1759–1771 (1993).
- Veazey, R.S. *et al.* Gastrointestinal tract as a major site of CD4<sup>+</sup> T cell depletion and viral replication in SIV infection. *Science* **280**, 427–431 (1998).
- Barber, S.A. *et al.* Longitudinal analysis of simian immunodeficiency virus (SIV) replication in the lungs: compartmentalized regulation of SIV. *J. Infect. Dis.* **194**, 931–938 (2006).
- Le Tortorec, A. & Dejuicq-Rainsford, N. HIV infection of the male genital tract—consequences for sexual transmission and reproduction. *Int. J. Androl.* **33**, e98–e108 (2010).
- Le Tortorec, A. *et al.* Human prostate supports more efficient replication of HIV-1 R5 than X4 strains *ex vivo*. *Retrovirology* **5**, 119 (2008).
- Shehu-Xhilaga, M. *et al.* The testis and epididymis are productively infected by SIV and SHIV in juvenile macaques during the post-acute stage of infection. *Retrovirology* **4**, 7 (2007).
- Miller, C.J. Localization of simian immunodeficiency virus-infected cells in the genital tract of male and female rhesus macaques. *J. Reprod. Immunol.* **41**, 331–339 (1998).
- Chacko, A.M. *et al.* Targeted delivery of antibody-based therapeutic and imaging agents to CNS tumors: crossing the blood-brain barrier divide. *Expert Opin. Drug Deliv.* **10**, 907–926 (2013).
- Barton, K.M., Burch, B.D., Soriano-Sarabia, N. & Margolis, D.M. Prospects for treatment of latent HIV. *Clin. Pharmacol. Ther.* **93**, 46–56 (2013).
- Chun, T.W. & Fauci, A.S. HIV reservoirs: pathogenesis and obstacles to viral eradication and cure. *AIDS* **26**, 1261–1268 (2012).
- Hill, A. Optimizing HIV treatment. *Curr. Opin. HIV AIDS* **8**, 34–40 (2013).
- Zhou, T. *et al.* Structural basis for broad and potent neutralization of HIV-1 by antibody VRC01. *Science* **329**, 811–817 (2010).
- Andrieux-Meyer, I. *et al.* Preferred antiretroviral drugs for the next decade of scale up. *J. Int. AIDS Soc.* **15**, 17986 (2012).
- Haase, A.T. Early events in sexual transmission of HIV and SIV and opportunities for interventions. *Annu. Rev. Med.* **62**, 127–139 (2011).

## ONLINE METHODS

**Antibody production.** The monoclonal antibody secreting hybridoma (clone 7D3) was provided by J.H.<sup>13</sup>. Preparation and purification of 100 mg of 7D3 was performed by R. Mittler of the Emory CFAR Immunology Core using standard methods. The isotype control antibody was purchased from Innovative Research, catalog # IR-MS-GF-ED (Endotoxin Depleted Mouse IgG).

**Antibody modification for *in vivo* imaging.** To conjugate 1,4,7,10-tetraazacyclododecane-1,4,7,10-tetraacetic acid mono (DOTA NHS) and poly(ethylene glycol) esters (PEG ester) to surface lysine residues of 7D3, molar ratios of 60:1 and 20:1, respectively, were used. Briefly, 1 mg of clone 7D3 mAb (at 3.8 mg/ml) was buffer exchanged with 0.1 M phosphate buffer (EMS), pH 7.3, plus Chelex 100 (Bio-Rad) using a 10-kDa Amicon spin column (Millipore). Then 1  $\mu$ l of 0.5 M DOTA NHS ester (Macrocyclics) in phosphate buffer and Chelex 100 and 32  $\mu$ l of 5 mM m-PEG-SMB 10K (Nectar), also in phosphate buffer and Chelex 100, were added and reacted for 4 h at RT on a rotator. Unconjugated reagents were removed using 30-kDa Amicon spin columns in phosphate buffer plus Chelex 100. Samples were quantified via UV-VIS spectroscopy, and the conjugations verified via gel electrophoresis using Tris-acetate gels in TA running buffer with SDS (Invitrogen). The modified 7D3 antibody was then divided into aliquots and lyophilized for storage.

**Radiolabeling.** Lyophilized PEG-DOTA-7D3 was resuspended in Chelexed 0.1 M  $\text{NH}_4\text{OAc}$ , pH 5.5 (Sigma). Copper (II)-64 chloride (Washington University) was diluted similarly; they were then mixed together at a ratio of approximately 5 mCi/mg and incubated at 37 °C for 1 h. The antibody conjugates typically labeled in the range of 1–3.5 mCi/mg per dose. Each dose was buffer exchanged with pharmaceutical-grade saline three times using a 10-kDa centrifugal filter to a final volume of 20  $\mu$ l. The conjugated mAb was then added to 1 ml of pharmaceutical-grade sterile saline in a sterile glass vial. Uptake was confirmed on an aliquot using thin layer chromatography. The labeled antibody conjugates gave values in the range of 1–3.5 mCi/mg.

***In vitro* 7D3-PEG-<sup>64</sup>Cu-Dota probe specificity test.** SIV1C cells with one integrated copy of SIVmac251 and uninfected parental Hut78 cells (ATCC TIB-161) were cultured in RPMI 1640 supplemented with penicillin-streptomycin and 10% FBS. 24 h before assaying, the cell cultures were supplied with 100 U/ml of rMamu IL-2-Fc to induce increased expression of SIV Gp120 on the surface of SIV1C cells<sup>34</sup>. For staining, tubes were set up with 500,000 cells containing varying mixtures of SIV1C and Hut78 cells (100%, 75%, 50%, 25% and 0% SIV1C). 200 ng of freshly radiolabeled 7D3-PEG-<sup>64</sup>Cu-DOTA were added to each tube of cells suspended in 200  $\mu$ l of PBS and incubated for 15 min at room temperature. The tubes were then washed three times with 2 ml of PBS and read in a Packard gamma counter. All cell lines used were free of mycoplasma.

**Competition of ‘cold’ 7D3-PEG-DOTA with 7D3-PEG-<sup>64</sup>Cu-DOTA.** 250,000 SIV-1C or control Hut78 cells were suspended in tubes with 200 ng of radiolabeled 7D3-PEG-<sup>64</sup>Cu-DOTA followed by the immediate addition of varying amounts of cold 7D3-PEG-DOTA (0, 56.3, 237.5, 950 and 3,800 ng). Incubation,

washing and reading of the tubes radioactivity were done as described above.

***Ex vivo* labeling of primary cells with 7D3-PEG-<sup>64</sup>Cu-DOTA.** Cryopreserved lymph node cells and splenocytes from both SIV-positive and SIV-negative rhesus macaques collected at necropsy were thawed, washed in PBS and counted. 5 million cells for each tissue were suspended in 200  $\mu$ l PBS and 500 ng of 7D3-PEG-<sup>64</sup>Cu-DOTA, and 10  $\mu$ l of serum from an SIV negative animal that were heat inactivated for 30 min at 56 °C. The cells were then incubated for 15 min at room temperature followed by four washes with 2 ml of PBS and read in a Packard gamma counter.

**Detection of 7D3-PEG-<sup>64</sup>Cu-DOTA on viral pellets.** At the time of imaging, blood was collected in citrate CPT tubes, which were processed according to vendor instructions (BD Biosciences). 1 ml of the resulting plasma was centrifuged at 21,130g for 1 h at 4 °C to pellet virus. The plasma was removed, and the pellet was washed with 1 ml of PBS twice and centrifuged again. After the final wash the pellet read in a gamma counter.

***In vitro* assay for serum modulation of probe binding.** Aliquots of 500,000 SIV1C cells or Hut78 cells were incubated at room temperature for 15 min with 200 ng of 7D3-PEG-DyLight 650 and 50  $\mu$ l of PBS, SIV pre-infection or SIV post-infection serum. Cells were then washed twice with 2 ml of PBS with 2% FBS. Cells were fixed with 200  $\mu$ l of 1% PFA in PBS and read on an LSR-II flow cytometer (BD). The data were analyzed using FlowJo software (Tree Star).

**Immunofluorescence detection of probe binding.** The ability of the 7D3-PEG-DOTA to bind Gp120 was tested via immunofluorescence in SIV1C (SIV positive)<sup>35</sup> or control Hut78 cells. Cells were cytopun onto glass slides, fixed and permeabilized in 50% methanol/acetone for 10 min at –20 °C, blocked with 5% BSA and stained using 10 ng/ $\mu$ l PEG-DOTA-7D3 and a Cy3-conjugated AffiniPure Donkey anti-mouse secondary antibody (#715-165-150, Jackson ImmunoResearch). The 7D3-PEG-650 used for flow cytometry measurements was also tested via immunofluorescence using the same protocol and showed a similar ability to bind Gp120.

**Probe modification for fluorescence measurements.** In order to conjugate PEG ester and DyLight 650 NHS ester (Thermo Scientific) to surface lysine residues of 7D3, 20:1 and 4:1 molar ratios, respectively, were used. Briefly, 1 mg of 7D3 was buffer exchanged with 0.1 M phosphate buffer using a 10-Da Amicon spin column. 32  $\mu$ l of 5 mM PEG and 1.12  $\mu$ l of 25 mM DyLight 650 were added and reacted for 2 h at RT on a rotator. Unconjugated reagents were removed using 30-Da Amicon spin columns in phosphate buffer. Samples were quantified via UV-Vis spectroscopy and stored at 4 °C.

**Monkeys.** A total of 14 adult Indian rhesus macaques age 5–11 years were used in this study as outlined in **Supplementary Table 1**. All animals were born at Yerkes National Primate Research Center and were maintained at the Yerkes National Primate Research Center of Emory University in accordance with the regulations of

the Guide for the Care and Use of Laboratory Animal, 8<sup>th</sup> edition. The experiments were approved by the Emory Institutional Animal Care and Use Committee as well as biosafety review board. Each of the animals used in the studies reported herein was inoculated with 200 TCID<sub>50</sub> (50% tissue culture infective dose) of SIV<sub>MAC239</sub> intravenously and served as a source for blood and tissues at various time points post-infection. All animals were typed for *MAMU-A\*001*, *MAMU-B\*008* and *MAMU-B\*017* alleles (**Supplementary Table 1**), and their plasma viral loads determined by qRT-PCR by the Emory CFAR Virology Core<sup>36,37</sup>. Of note, none of the EC monkeys expressed *MAMU-B\*008* or *MAMU-B\*017*, traditionally associated with increased control of viremia<sup>38,39</sup>.

**PET/CT imaging.** Animals were imaged using a Siemens Biograph 40 PET/CT, using image settings for <sup>64</sup>Cu. Typically between 250 and 300 slices were compiled for each macaque depending on body size.

**Necropsy.** Animals showing signs of disease or distress or that reached IACUC end points, such as pain or stress that could not be alleviated using standard analgesics and/or chemotherapy were humanely euthanized with an intravenous overdose of pentobarbital sodium according to the guidelines of the American Veterinary Medical Association. A complete necropsy was performed on these animals. For histopathologic or immunohistochemical examination, various tissue samples were fixed overnight in 4% paraformaldehyde, embedded in paraffin and sectioned at 4 μm.

**Biopsy.** Animals were anesthetized with either ketamine (5–10 mg per kg body weight (mg per kg), intramuscular) or Telazol (3–5 mg per kg, intramuscular) and placed in ventral or lateral recumbency, and a lubricated anoscope was introduced into the rectum. Feces were removed using clean cotton tipped applicators. Up to 20 colorectal biopsies per collection were obtained using a biopsy forceps under visualization. The procedure is generally well tolerated and does not require analgesics. The colorectal biopsies were collected in RPMI 1640 with gentamicin at 4 °C. They were then removed from media weight in tared tubes and read on the Packard gamma counter.

**PET image analysis.** PET/CT fusions were analyzed using OsiriX software on a MacBook Pro or Mac Pro. The volume ROI tool was extensively used to measure standard uptake values (SUVs), SUV<sub>max</sub> and SUV<sub>mean</sub> within a specific organ. In order to evaluate the voxel fraction with uptake, the 3D images from OsiriX were exported as TIFF stacks and imported into PerkinElmer Volocity software. Within Volocity, 3D ROIs were created to represent the GI tract; the mean uptake of the GI tract was measured, the total volume, as well as the voxel fraction (volume fraction) of objects with SUV values between 1.0 and 3.3 within the GI tract. For each imaging experiment presented, SUVs were compared at the same time point injection of the radiotracer. Haralick texture features<sup>40</sup> were computed using an ImageJ plug-in or in Matlab.

**Statistical methods.** This manuscript describes three experiments: (i) a comparison of PET SUV<sub>max</sub> measurements in chronically infected macaques and uninfected macaques and measurements in uninfected macaques using an isotype control modified

antibody; (ii) a comparison of SUV<sub>max</sub> measurements in three animals, all chronically infected with SIV, imaged with PET, treated with ART for 4 weeks and then imaged again via PET; and (iii) PET imaging in ECs (>5 years aviremic), chronically infected animals and uninfected control animals. The results from these three experiments have been analyzed using two statistical approaches. First, a global comparison of the PET measurements for each animal state was performed that included the measurements of all of the organs. This was achieved applying a fully nested hierarchical ANOVA model (implemented in Matlab (MathWorks)) for the SUV<sub>max</sub> response  $y_{ijk} = \mu + \alpha_i + \beta_{j(i)} + \gamma_{k(j)} + \epsilon_{ijk}$ , where  $y_{ijk}$  is the SUV<sub>max</sub>,  $\alpha$  is the effect of the infection status,  $\beta$  the effect of animal nested in status, and  $\gamma$  is the effect of the organ system nested in each animal. In the model discussed above, Q-Q plots of residuals of the proposed model against Gaussian quantiles for each experiment exhibited a linear pattern clearly indicating that the assumption of normality of the SUV<sub>max</sub> measurements was appropriate. In addition, a Kruskal-Wallis, Bonferroni-ANOVA, or Wilcoxon–Mann-Whitney test was applied, which enabled the analysis of each organ separately comparing the differences in that organ's measurement for each animal state.

**Sample size and exclusions.** Groups of 4 monkeys were used for analyses, with viral loads in comparable ranges. For the ART group, 3 animals are shown (a fourth developed AIDS during treatment and was euthanized). However, these comparisons are within the same animal before and after therapy. A total of 8 viremic monkeys were tested (including pre-ART values), 4 elite controllers, and 2–4 uninfected controls for background values. (**Supplementary Table 1**). No sample-size estimates were performed to ensure adequate power to detect a prespecified effect size.

**Randomization and blinding.** The grouping was based on plasma viral loads (viremic:  $3 \times 10^4$  to  $\sim 3 \times 10^6$  viral rRNA copies per ml of plasma; ECs and ART treated: <60 copies vRNA per ml of plasma). No other randomization was utilized. Male and female monkeys were utilized (**Supplementary Table 1**). No blinding was utilized.

**Quantitative RT-PCR.** Plasma and tissue RNA was isolated using the QiaAmp Viral RNA Mini-Kit and RNeasy Mini Kit, respectively (Qiagen). Viral RNA (vRNA) levels were measured by qRT-PCR; the assay sensitivity was 60 vRNA copies per ml for plasma, and RNA copy numbers in tissues were normalized per ng of total RNA and represented as SIV RNA copies per ng of total RNA.

**IHC in tissue sections.** Immunohistochemical staining was performed using an alkaline phosphatase–streptavidin–biotin procedure. Tissues collected by biopsy/necropsy were fixed overnight in 4% paraformaldehyde, embedded in paraffin and sectioned at 4 μm. Paraffin-embedded sections were subjected to deparaffinization in xylene, rehydration in graded series of ethanol, and rinsed with distilled water. Antigen retrieval was performed by immersing sections in a target retrieval solution (Dako) at 120 °C for 30 s in a steam pressure declouding chamber (Biocare Medical). The slides were then allowed to cool for 20 min, washed with distilled water, and placed in Tris buffer saline (Sigma) for 5 min. Sections were then blocked with Protein Block, Serum-Free (Dako) for 15 min. The primary monoclonal antibody (SIVmac p27 monoclonal antibody (FA2), NIH AIDS Reagents Program) was diluted in antibody diluent (Dako) at

room temperature. The sections were incubated with the primary mAb overnight in a humidified chamber at 4 °C followed by biotinylated rabbit anti-mouse antibody (#E035401-2, Dako) and alkaline phosphatase–streptavidin conjugate (#S-921, Invitrogen) for 30 min each at room temperature. Following each incubation, the slides were washed with Tris buffer saline containing Tween 20 (Sigma). Antibody labeling was visualized by development of the chromogen (Vulcan Fast Red; Biocare Medical). The reaction was stopped by immersing the slides in distilled water, and nuclei were counterstained using Gill's hematoxylin. Digital images of Vulcan Fast Red–stained slides were captured at 400× magnification with an Olympus BX43 microscope equipped with a digital camera (DP26, Olympus) using cellSens digital imaging software 1.9 (Olympus). Positive controls included samples of spleen and lymph node from SIV-infected rhesus macaques. Negative control, colon, was performed by omitting the primary mAb.

34. Lairmore, M.D., Post, A.A., Goldsmith, C.S. & Folks, T.M. Cytokine enhancement of simian immunodeficiency virus (SIV/mac) from a chronically infected cloned T-cell line (HuT-78). *Arch. Virol.* **121**, 43–53 (1991).
35. Daniel, M.D. *et al.* Isolation of T-cell tropic HTLV-III-like retrovirus from macaques. *Science* **228**, 1201–1204 (1985).
36. Hong, J.J., Amancha, P.K., Rogers, K., Ansari, A.A. & Villinger, F. Spatial alterations between CD4<sup>+</sup> T follicular helper, B, and CD8<sup>+</sup> T cells during simian immunodeficiency virus infection: T/B cell homeostasis, activation, and potential mechanism for viral escape. *J. Immunol.* **188**, 3247–3256 (2012).
37. Hong, J.J., Amancha, P.K., Rogers, K., Ansari, A.A. & Villinger, F. Re-evaluation of PD-1 expression by T cells as a marker for immune exhaustion during SIV infection. *PLoS ONE* **8**, e60186 (2013).
38. Torriani, M. *et al.* Increased FDG uptake in association with reduced extremity fat in HIV patients. *Antivir. Ther.* **18**, 243–248 (2013).
39. Yant, L.J. *et al.* The high-frequency major histocompatibility complex class I allele *Mamu-B\*17* is associated with control of simian immunodeficiency virus SIVmac239 replication. *J. Virol.* **80**, 5074–5077 (2006).
40. Haralick, R.M., Shanmugam, K. & Dinstein, I. Textural features for image classification. *IEEE Trans. Syst. Man Cybern.* **3**, 610–621 (1973).



## Erratum: Whole-body immunoPET reveals active SIV dynamics in viremic and antiretroviral therapy-treated macaques

Philip J Santangelo, Kenneth A Rogers, Chiara Zurla, Emmeline L Blanchard, Sanjeev Gumber, Karen Strait, Fawn Connor-Stroud, David M Schuster, Praveen K Amancha, Jung Joo Hong, Siddappa N Byrareddy, James A Hoxie, Brani Vidakovic, Aftab A Ansari, Eric Hunter & Francois Villinger

*Nat. Methods* 12, 427–432 (2015); published online 9 March 2015; corrected after print 11 June 2015

In the version of this article initially published, the first name of Emmeline L. Blanchard was misspelled as Emeline. The error has been corrected in the HTML and PDF versions of the article.